Full Length Article

How positioning of a hard ceramic TiB$_2$ layer in Al/CuO multilayers can regulate the overall energy release behavior

Vidushi Singh [a], Tao Wu [a], Erik Hagen [b], Ludovic Salvagnac [a], Christophe Tenailleau [c], Alain Estéve [a], Michael R. Zachariah [b], Carole Rossi [a,*]

[a] LAAS-CNRS, University of Toulouse, 7 Avenue du colonel Roche, 31400 Toulouse, France
[b] University of California, Riverside, CA 92521, USA
[c] CIRIMAT, Université de Toulouse, CNRS, Université Toulouse 3 - Paul Sabatier, 118 Route de Narbonne, 31062 Toulouse Cedex 9, France

ABSTRACT

This study reports on a new ternary thermite comprising of Al-TiB$_2$/CuO multilayers, designed to take the advantage of high ignitability of titanium (Ti), high volumetric density of boron (B), and low melting point of aluminum (Al). Results demonstrate synergetic effects leading to an energetic layer outperforming its single fuel counterparts, Al/CuO or TiB$_2$/CuO, while being safe to handle. The additive TiB$_2$ not only lowers the ignition energy by 100%, but also enhances the burn rate by more than a factor of two compared to the single fuel samples (Al/CuO and TiB$_2$/CuO). The thermite reaction sequences and synergy of Ti, B and Al oxidation, examined by thermo-analytical analyses coupled with X-ray spectroscopy and high-resolution electron energy loss spectroscopy, demonstrate the strong affinity of TiB$_2$ to oxygen that catalyzes CuO decomposition at temperatures as low as 380 °C; followed by a dual-step TiB$_2$ oxidation: first to TiO, and then to TiO$_2$ led by a reaction limiting step of oxidizer availability. Finally, Al undergoes oxidation via liquid boron oxide as well as gaseous oxygen. This study also underlines the crucial effect of the nanolayer morphology in the thin-film technology: when Al is sputter-deposited onto the TiB$_2$ layer, Al ions penetrate into the grain boundaries penalizing TiB$_2$ reactivity. The results demonstrate the advantages of using TiB$_2$ fuel to improve the ignitability and the combustion performance of Al based thermite and offer some means to finely tune the energetic properties.

1. Introduction

Metal-based reactive materials have long been explored and developed as the next-generation energetic materials and may benefit various applications that includes additives to propellants and pyrotechnics [1–4], high temperature material synthesis [5,6] as well as micro-initiation [7–13]. One of the most promising reactive materials emerged in the 2000s is nanothermite which combines a metal and a metal oxide at nanoscale to chemically release large amounts of heat. These nanoscale energetic materials possess high volumetric energy densities (up to 80 kJ.cm^{-3}), high adiabatic flame temperatures (>2600 °C) and improved combustion properties by several times [14–19] compared to the microscale counterparts. A number of factors, in addition to the components' (metal and metal oxide) nature, influence the combustion properties of these reactive materials: they include the components' size, their intimacy, the metal/metal oxide interfacial layer's nature and thickness, as well as the metal and metal oxide mass

ratio, thus providing quite a few ways to manipulate the overall energetic performance. Aluminum (Al) is still predominantly the metal of choice because of its high oxidation enthalpy, non-toxic nature, abundance and low cost [20–24]. However, its low melting point leads to sintering process prior the thermite initiation curtailing the reaction surface area [25–29], and the presence of native alumina on aluminum fuel negatively impacts its ignitability. To overcome these shortcomings, a variety of alloys or binary fuels i.e. a combination of Al and a second metal such as Zr, Mg, Ti and B chosen for their gravimetric or volumetric energy density, have been examined [30–33] with significant interest in ignition/combustion characteristics.

For example, ignition temperatures of Al-Zr or Al-Mg binary fuels are significantly lower than those of pure Al of similar sizes due to the exothermic reactions of formation of intermetallic phases (Al + Mg and Al + Zr) that drives the thermite ignition at very low temperatures (~350 °C) [34,35]. Compared to Al-Zr and Al-Mg binary fuels, Al-Ti ones offer the potential for very low ignition thresholds, higher

gravimetric heats of combustion, and lower costs. For example, Shoshin et al. found that ball-milled Al-Ti powders burn relatively faster than their pure counterparts of similar sizes [36]. Very recently Wu et al. reportedly established the strong oxygen affinity of Ti at low temperature (300 °C) together with extreme sensitivity [37] which makes Ti based thermite difficult to handle safely. Another fuel to have attracted a lot of attention is Boron (B) due to its very high volumetric and gravimetric energy density [38,39], sustainability and low cost.

Undoubtedly, a combination of B and Ti with Al fuel should lead to promising new thermite composition by coupling the advantage of each material (**Table S1, Supplementary Information**). The technological objective of this paper is to develop a thin-film technology to produce ternary fuel thermite nanolaminates, e.g. Al-TiB$_2$/CuO multilayers, with controlled bilayer spacing and featuring reduced ignition delays, shorter burn times, higher combustion temperatures, compared to traditional single fuel Al/CuO nanolaminates [40–45] while being as safe to handle. CuO was chosen for its strong oxidizing nature. The scientific objectives are two-fold: (i) examine the initiation and the combustion behavior of CuO/TiB$_2$-Al and CuO/Al-TiB$_2$ nanolaminates, using high-resolved and high-speed visible and infrared camera; and, (ii) depict the sequential reactional steps combining thermal analysis, X-ray diffractometry, high-magnification Transmission Electron Microscopy (TEM) and Scanning Transmission Electron Microscopy (STEM), with a High-Angle Annular-Dark-Field (HAADF) mode, to probe the chemical and the structural evolution of different interfaces upon heating with ultra-high spatial resolution. The advantages of using Al-TiB$_2$ fuel are clear in terms of its capability of tuning both the ignitability and the combustion via TiB$_2$ incorporation in the multilayer stack. Moreover, the position of TiB$_2$ nanolayer in the thin film stack only has a slight effect on the ignition and the combustion properties.

2. Materials and methods

2.1. Sample preparation

CuO, TiB$_2$, Al nanolayers were deposited using Direct Current (D.C.) magnetron sputtering from Neyco, France purchased 99.99% purity, 8 by 3 square inches and ¼ inch thick Cu, TiB$_2$ and Al targets in an equipment from Thin Film Equipments (TFE), Italy. Prior to the deposition of each nanolayer, the chamber was pumped down to 2×10^{-7} torr followed by the introduction of the gases. The gas flow was set via percent-flow control as described in our previous works [46]. Briefly, the argon flow was set to 100% during each of the sputtering event, except CuO, wherein the percent flow of each of the two gases, oxygen and argon was set to 50% resulting in 22.5 s.c.c.m. Ar gas flow and 32 s.c.c.m. oxygen gas flow. The sputtering process conditions are summarized in **Table S2, Supplementary Information**. The unbiased sample holder was centered 15 mm away from the target. The chamber was pumped down, and a cooling time for the sample holder was applied prior to each subsequent sputtering event.

Various multilayers were prepared to perform a head-to-head comparison. Each stack was composed of 10 bilayers (BL) of CuO/Me {Me: TiB$_2$-Al, Al-TiB$_2$, TiB$_2$, Al}, the latter two respectively serving as the reference samples. All the multilayers began with CuO followed by the deposition of the metallic layer. TiB$_2$-Al signifies the deposition of TiB$_2$ (over CuO) followed by that of Al on TiB$_2$, whereas Al-TiB$_2$ notation represents the deposition of Al (over CuO) followed by that of TiB$_2$ on Al. In each multilayer, a fuel rich configuration (phi = 2) was used and the CuO layer thickness was set to 200 nm. Phi is defined as the molar ratio between the fuel (Al/TiB$_2$) and the oxidizer (CuO). Hence, the corresponding thicknesses of TiB$_2$ (in CuO/TiB$_2$) and the respective thicknesses of TiB$_2$ and Al (in CuO/TiB$_2$-Al and CuO/Al-TiB$_2$) are 100 nm, 62 nm and 80 nm. As for the remaining reference sample, the resultant Al layer thickness is 200 nm. In addition, one bilayer of CuO/TiB$_2$-Al and CuO/Al-TiB$_2$ finished with a CuO layer on top was prepared on Si substrate to perform the interface analysis. The thickness of each nanolayer

is carefully controlled via a calibration process preceding each full stack deposition. Additionally, 2 BL samples of CuO/Me were prepared on Si substrate to perform annealing experiments. CuO-TiB$_2$-Al-CuO and CuO-Al-TiB$_2$-CuO multilayers were also sputter deposited on Si substrate to analyze the microstructural evolution of the two systems close to each of the interfaces.

For combustion tests, lines of 10 BL CuO/Me with dimensions of 25 mm (length) × 2 mm (width) were sputter deposited through a shadow mask onto a 500 μm thick glass slide and ignited using a resistively heated titanium (Ti) filament. Prior to thermite deposition, a photolithography process was used to pattern 300 nm thick Ti resistors on 4-inch glass wafers. Au (800 nm thick) was evaporated onto the surface and patterned thereafter to define the Ti filament as well as the Au electrical contact pads. For ignition tests, a similar fabrication process was followed except the multilayers were deposited using a different shadow mask, with an active thermite area of 5.6 × 6.7 mm^2.

Finally, free standing 10 BL of CuO/Me were also fabricated for ignition threshold characterization and thermal analysis. A silicon wafer was subjected to plasma cleaning following which a layer of photoresist (NLOF, 5 μm) was spin-coated. Succeeding a post-exposure 110 ℃ baking (PEB) step, the multilayers were sputtered onto the wafer. The multilayer foils were then released by dissolving the photoresist in acetone.

2.2. Material characterization

The crystallographic structure of each nanolayer and the phase was determined using SIEFERT XRD 3000 TT X-Ray diffractometer with Cu-Kα radiation (λ = 1.5406 Å) fitted with a diffracted beam graphite monochromator. The 2θ X-Ray Diffraction (XRD) measurements were performed from 10° to 60° with a step of 0.04°. The morphology and the chemical composition of the multilayers were analyzed by Scanning Electron Microscopy (SEM), Transmission Electron Microscopy (TEM), Scanning Transmission Electron Microscopy (STEM) and Electron Energy Loss Spectroscopy (EELS) using a JEOL cold-FEG JEM-ARM200F operated at 200 kV equipped with a probe Cs corrector reaching a spatial resolution of 0.078 nm. EELS data were acquired on a Gatan imaging filter quantum (energy resolution of 0.3 eV) using a dispersion of 0.5 eV/channel, a collection angle of 29.4 mradians and a semi convergence angle of 14.8 mradians. The spatial resolution was estimated at 0.5 nm. FEI Helios NanoLab DualBeam FIB-SEM was used to acquire morphological images as well as perform Focused Ion Beam (FIB) technique to prepare the cross-sectional lamellae.

The heat released during each step of the chemical reaction in the multilayers is characterized by thermal analysis performed in Ar atmosphere using a Differential Scanning Calorimetry (DSC) carried out in a NETZSCH DSC 404 F3 Pegasus system equipped with a DSC-Cp sensor type S and a Platinum furnace. The diffractogram, normalized to the foil mass (typically ∼ 10 mg), was recorded at a constant heating rate of 10 °C/min up till 950 °C and then baselined manually.

The slow annealing experiments were performed in high metals tube furnace (AET Technologies) at a heating rate of 10 °C.min^{-1} (same as that of DSC) and a cooling rate of 2 °C.min^{-1} under an inert N$_2$ atmosphere.

2.3. Ignition tests

Auto ignition temperature: A hot plate was utilized to understand the effect of high heating rate on the ignition event in the thermites and involved instantly heat the free-standing 10 BL CuO/Me foils. This method involves placing ∼1 mg of foils specimen in contact with the hot surface and observing the reaction (spark emission). Samples that fail to ignite when heated at that temperature do not emit a burst of light. Note that for each test, the hot-plate is held at a constant temperature and fresh multilayer specimens are dropped onto its surface. Enough time is allowed for the plate temperature to stabilize before each testing event. The test setup and the snapshots from the tests are shown in **Figure S1**,

Ignition energy: The multilayers were ignited using externally applied direct current pulse resistively heating the Ti filament in an ambient atmosphere. For each test, the current was adjusted so as to keep the same dissipated power (6.125 W). The ignition delay was measured using a photodiode (VISHAY, BPV10) biased at 5 V placed a few centimeters away from the sample and capable of detecting the optical flash emitted from the ignition event. A 1 kΩ dummy resistance was used to measure the photocurrent. The electrical setup is shown in **Figure S2, Supplementary Information**. All electrical signals were acquired on a digital oscilloscope and processed using in-house programs. Several tests were performed, and a mathematical average value of ignition delay (ms) was constituted. Results are then reported in terms of ignition energy calculated as the integral of power over time (up to initiation). The ignition delays can be found in **Table S3, Supplementary Information**.

2.4. Macro and microscopic imaging of combustion and flame temperature

The flame propagation speed was evaluated using a high-speed camera (VEO710, Phantom, USA) recording at 48,000 frames per second with a resolution of 512 × 64 pixels. The videoed films from multiple samples of each type were processed using Phantom Camera Control (PCC) Software to report the statistical values of average macroscopic burn rate. Briefly, 6 two-points measurements were performed to determine the propagation speed for each device across each of the four CuO/Me thermite stacks. Five devices from each configuration were tested. The macroscopic burn rate is then reported as a mathematical average for each multilayer. The setup to determine the front thickness and the flame temperature is comprised of a high-speed camera (Phantom VEO710L, USA) coupled with a long-distance microscopic lens (Infinity Photo-optical Model K2 DistMax, CF-4 Objective). At a pixel/distance ratio of ~2 μm/pixel, the propagation of the flame front was recorded at 60,000 frames per second. The thickness of the front is obtained from the optical micrograph recorded during the propagation event. The tool is calibrated to a blackbody source (Mikron M390) for color pyrometry to estimate the reaction temperatures. Further information about the pyrometry measurement can be found in previous studies [19]. Concisely, a raw temperature map is extracted using a three-color (RGB) channel and an average value of the flame temperature is obtained from several such points on the front. The error threshold on the reported values is about 200–300 K.

3. Results and discussions

3.1. Ignition, burn-rate and flame front characteristics

The first two columns of Table 1 give the ignition energy and global burn rate measured for CuO/TiB$_2$-Al and CuO/Al-TiB$_2$ stacks compared

Table 1
Ignition energy (mJ), burn rate (m.s^{-1}), ignition threshold (K) and flame characteristics of 10 BL CuO/Me {Me: Al, TiB$_2$, TiB$_2$-Al, Al-TiB$_2$}.

10 BL stacks	Ignition energy (mJ)	Burn rate (m. s^{-1})	Flame temperature (°C)	Auto-ignition point (°C)	Flame thickness (μm)
CuO/ Al	102.1 ± 15.6	4.3 ± 0.1	3500	700 ± 5	65
CuO/ TiB$_2$	5.9 ± 1.1	2.3 ± 0.04	1800	285 ± 1	592
CuO/ TiB$_2$-Al	1.3 ± 0.7	8.3 ± 0.3	3000	380 ± 1	83
CuO/ Al-TiB$_2$	0.3 ± 0.2	10.8 ± 0.5	3100	445 ± 1	85

to CuO/Al and CuO/TiB$_2$ reference multilayers samples. The ternary systems CuO/TiB$_2$-Al and CuO/Al-TiB$_2$ demonstrated much higher burn rates of 8.2 ± 0.31 m.s^{-1} and 10.8 ± 0.52 m.s^{-1} respectively, in comparison to the reference samples: CuO/Al and CuO/TiB$_2$, which burn at 4 ± 0.1 m.s^{-1} and 2.3 ± 0.04 m.s^{-1}, respectively. The additive TiB$_2$ not only enhances the burn rate by ~ 50% compared to the CuO/Al reference sample but also exhibited ~100% lower ignition energy of 1.3 mJ (CuO/TiB$_2$-Al) and 0.033 mJ (CuO/Al-TiB$_2$) in comparison to unary fuel-based reference nano-thermites. Clearly incorporating TiB$_2$ with Al (molar ratio 1:1) proved to be more reactive than both single fuel systems.

It is interesting to note that despite a lower auto-ignition temperature (~285 °C), CuO/TiB$_2$ possesses quite low burn rate indicating the thermite reaction is likely to be dominated by condensed phase thus inhibiting the forward energy transfer. The V-shaped flame front of CuO/TiB$_2$ burns dimly with little to no creation of particles (Fig. 1**b),** while the burning front of CuO/Al is characterized by particle emissions and intense bright light (Fig. 1**a)**. This implies a higher flame temperature as well as more gas generation [47] in the latter samples. Certainly, the flame temperature of CuO/Al is measured at 3500 °C, much higher compared to that of CuO/TiB$_2$ measured at 1800 °C, the latter being (Table 1) well below the melting point of TiB$_2$ (3230 °C), bringing another indication in of its combustion behavior in the condensed phase. The CuO/TiB$_2$ flame front thickness is also much thicker (~590 μm) compared to that of CuO/Al (64 μm) further supporting that the combustion is extended in the condensed phase that remains active long after the passing of the flame front. Fig. 1b shows the CuO/TiB$_2$ thermite still burning even after the passing of the flame front with no visible gas generation.

In bi-fuel thermites (TiB$_2$-Al and Al-TiB$_2$), we clearly distinguish two combustion stages as shown by the thin sharp well-defined V or slant-shaped front (Fig. 1**c-d)** strikingly different from slightly curved Al flame front. The first combustion stage is dominated by combustion of Al in the vapor phase, followed by the condensed phase combustion of TiB$_2$. Another observable characteristic difference is a less intense gas generation in the burning of the bi-fuels compared to Al/CuO burning: the bi-fuels exhibit particles tearing away from behind the flame front as it progresses. Among TiB$_2$-Al and Al-TiB$_2$ fuels, it seems that Al-TiB$_2$ displays superior reactivity than TiB$_2$-Al in that the propagation of the flame front generates more energy that then ejects smaller more uniform particles as opposed to larger string-like solid emissions from TiB$_2$-Al. This points to a faster energy transfer in Al-TiB$_2$ than that in TiB$_2$-Al, even though the flame front characteristics are very similar. CuO/TiB$_2$-Al and CuO/Al-TiB$_2$ feature similar flame front thicknesses (~80 μm) and flame temperatures (~3000 °C). We speculate that the likely cause of very low initiation points in bi-fuel thermites (CuO/TiB$_2$-Al and CuO/Al-TiB$_2$) may be the first stages of reaction, when the first oxides (TiO$_x$ and B$_x$O$_y$) in contact with CuO are formed, thus ensuing the reaction with the exposed fuel. In order to understand the nature of the exothermic events, foils from each configuration (CuO/TiB$_2$-Al, CuO/Al-TiB$_2$) as well as the reference samples (CuO/Al, CuO-TiB$_2$) were analyzed by DSC with a heating ramp of 10 °C.min^{-1} under a constant flow of Ar.

3.2. Thermo-analytical analysis

DSC traces of CuO/TiB$_2$-Al and CuO/Al-TiB$_2$ are plotted in Fig. 2 with those of CuO/Al and CuO/TiB$_2$ samples, obtained under the same conditions. DSC traces show exotherms of subsequent oxidation reactions of Al and TiB$_2$ with CuO without the contribution of oxygen from the surrounding environment. The total heat of reaction is indicated across each plot. To supplement the understanding of the different reaction steps, CuO/TiB$_2$-Al sample was annealed at 475 °C, 550 °C and 950 °C while CuO/Al-TiB$_2$ sample was annealed at 375 °C, 480 °C and 950 °C corresponding to the main peaks recorded in the DSC scan and their respective compositions were analyzed by XRD. The composition

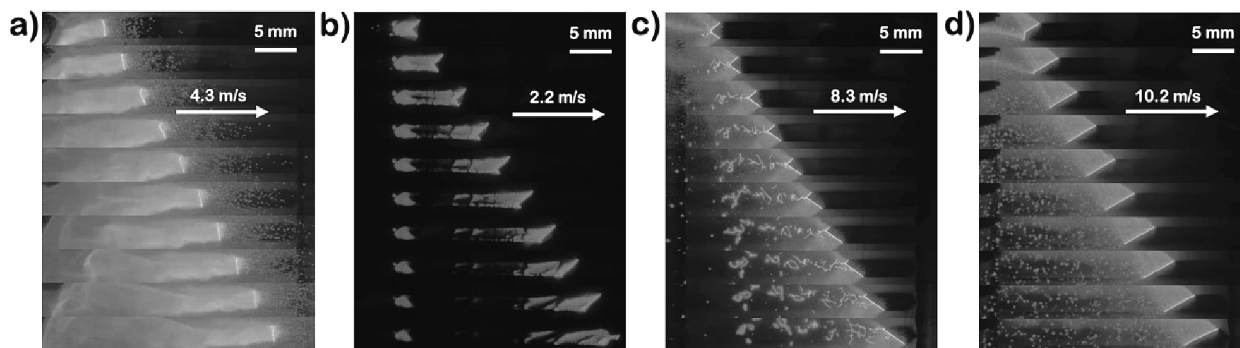**Fig. 1.** Snapshots from propagation of 10 BL CuO/Me {Me: **a)** Al, **b)** TiB$_2$, **c)** TiB$_2$-Al and **d)** Al-TiB$_2$}.
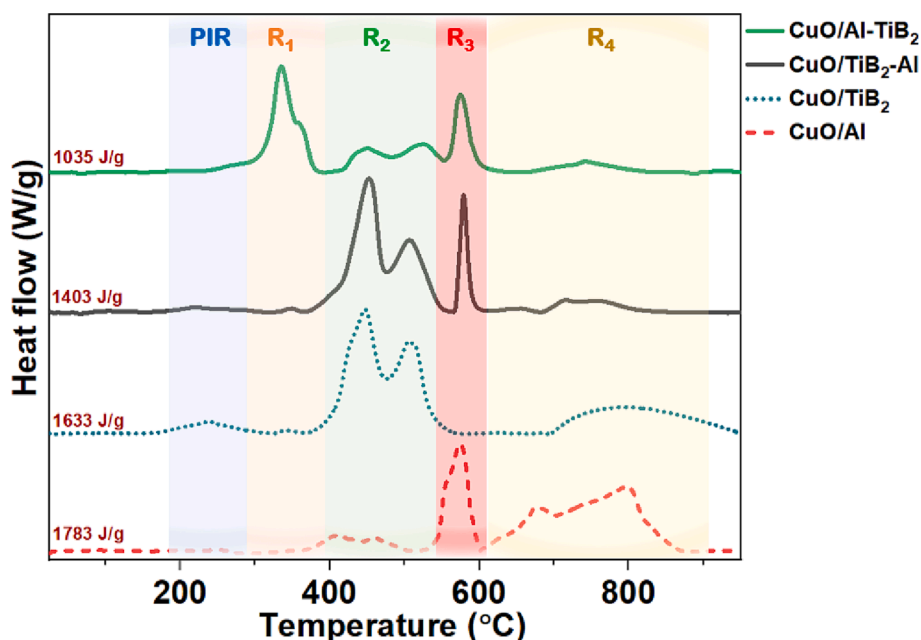

Fig. 2. DSC traces of 5 BL CuO/Me {Me: Al, TiB$_2$, TiB$_2$-Al}. The traces are baseline subtracted manually and are offset in Y to provide clarity. The plot is divided into 5 regions: a pre-ignition region (PIR), regions R$_1$, R$_2$, R$_3$ and R$_4$.

of each sample after annealing steps is summarized in Table 2 while the XRD diagrams can be found in **Figure S3, Supplementary Information**.

Even though the respective total heats of reaction of CuO/Al and CuO/TiB$_2$ exceed that of CuO/TiB$_2$-Al and CuO/Al-TiB$_2$, the phenomenon must be carefully analyzed as important differences in the occurrences of the exotherms when TiB$_2$ is added to CuO/Al multilayer are observed. Therefore, each of these ternary systems is systematically compared and analyzed with the former reference samples as follows.

CuO/TiB$_2$-Al system: The DSC scan (Fig. 2, black trace), shows a tiny exothermic peak (onset temperature of ~200 °C) attributed to the

Table 2
Summary of chemical constituents of as deposited (AD) and annealed CuO/Me {Me: Al, TiB$_2$, TiB$_2$-Al}.

Sample	Constituents at different temperatures			
	AD	475 °C	550 °C	950 °C
CuO/TiB$_2$	CuO, TiB$_2$	TiO$_2$, Cu$_2$O	Ti$_x$Cu$_y$, Cu$_2$O, Cu	Ti$_x$Cu$_y$, Cu
CuO/ TiB$_2$-Al	CuO, Al, TiB$_2$	TiO$_x$, Cu$_2$O, AlTi, Al, Cu	B, Al, TiO$_2$, Cu$_2$O, Cu, Ti$_x$Cu$_y$	Ti$_x$Cu$_y$, Cu
CuO/Al-TiB$_2$	CuO, Al, TiB$_2$	TiO$_2$, Cu$_2$O, B$_2$O$_3$, Cu	TiO$_2$, Cu$_2$O, B$_2$O$_3$, B, Cu, Ti$_x$Cu$_y$	Ti$_x$Cu$_y$, Cu

reactions occurring prior to ignition indicated in the pre-ignition region (PIR) that lead to the formation of TiO$_x$ starting at 300 °C [37]. As a matter of fact, at 200 °C, condensed-phase oxygen transfer is thought to occur until CuO begins to decompose at ~350 °C [48]. In ~ 375–550 °C range (Fig. 2, region R$_2$), an apparent exothermic double peak (onset temperature of ~ 380 °C) is seen, which is due to the oxidation of TiB$_2$ forming two oxide layers: liquid B$_2$O$_3$ and TiO$_2$, as the oxygen atoms migrate outwards following the release from the decomposition of CuO. The XRD of samples annealed at 475 °C confirms the presence of TiO$_2$, B$_2$O$_3$ and Cu$_2$O, the latter confirming the early decomposition of CuO (Table 2). This exothermic double peak is a succession of two exotherms, corresponding to the oxidation of TiB$_2$ resulting in two adjacent native oxides (TiO$_x$-B$_2$O$_3$), separated by the melting of boric oxide at ~450 °C. It is noteworthy that as the sample approaches the melting temperature of B$_2$O$_3$, some of the released heat is consumed in melting the oxide bringing the exotherm down. Further temperature increase leads to the second peak of this first exotherm at 505 °C (onset at 470 °C) which is the continuation of TiB$_2$ oxidation. XRD analysis after annealing at 550 °C stages the presence of TiO$_2$, Cu$_2$O and Cu. Overall, this two-step TiB$_2$ oxidation produces 79.5% of the total heat released in the ambient – 950 °C range, i.e., 1116 J.g^{-1} of 1400 J.g^{-1} total released heat. Next, region R$_3$ relates to the main CuO-Al oxidation reaction [46]. It releases much lower heat compared to the reference CuO/Al sample. This might

be due to the tendency of Ti atoms to rapidly react and consume oxygen compared to that of Al [37] as previously reported. As for the last peaks in region R_4, similar to CuO/Al, the exotherm simply relates to Al oxidation in both the gas and the condensed phase [49]. It should be noted that a Cu signal is observed in XRD (**Figure S3b-c, Supplementary Information**) that evidently supports the superior reactivity of TiB$_2$-Al as well as Al-TiB$_2$ bi-fuel systems in that the main reaction is catalyzed compared to Al-only thermite. The peaks corresponding to boric oxide are quite low intensity which is likely due to its materialistic nature.

CuO/Al-TiB$_2$ system: A noteworthy feature of CuO/Al-TiB$_2$ (Fig. 2, green plot) is the major low temperature exotherm (onset of ∼ 230 °C) (region R_1) which produces ∼ 45% of the total heat of reaction (455 J. g^{-1} of 1035 J.g^{-1} total released heat) and the quenched subsequent exothermic double peak (region R_2). This first exotherm is attributed to the rapid consumption of oxygen atoms released as a result of CuO decomposition by TiB$_2$ to form TiO$_x$. XRD analysis at the end of the first exotherm (380 °C) shows the presence of Cu$_2$O and TiO$_2$ which in turn confirms this event. Quite conspicuously, the presence of TiB$_2$ between each Al/CuO bilayer seems to catalyze the oxygen release from CuO slightly faster than its presence sandwiched between CuO and Al. This low temperature exotherm seems to be responsible for the lowest ignition onset in this system (ignition point measured at 285 °C, Table 1). With most of TiB$_2$ already oxidized in the PIR + R_1 region, there is less oxygen atoms to further diffuse through the native oxides of TiB$_2$ to oxidize the core leading to the first peak of region R_2 around the same temperature as CuO/TiB$_2$-Al system. Similarly, the following exotherm in this region post B$_2$O$_3$ melting results in the remaining of the oxidation event. Finally, region R_3 represents CuO-Al oxidation reaction. Post annealing at 550 °C, unlike CuO/TiB$_2$-Al system, XRD of CuO/Al-TiB$_2$ reveals the presence of elemental boron and severe Cu-Ti alloying. The presence of Cu$_2$O upholds the ongoing CuO/Al thermite reaction at this stage (Region R3, Fig. 2). Region R_4 is characterized by low heat events attributed to little to no presence of the oxidizer, as well as alloying of Ti and Cu.

Finally, for both samples, CuO/Al-TiB$_2$ and CuO/TiB$_2$-Al, more intense the low temperature peaks, less is the high temperature Al oxidation exotherms (Fig. 2, region R_3 and R_4), confirming a lower availability of Al during this last event, as it was consumed during the first low temperature events.

Overall, the analysis of the exothermal events brings about three salient findings:

(i) Addition of TiB$_2$ to Al/CuO modifies the low temperature reaction steps, i.e. those occurring below Al melting, which explains the superior reactivity in term of prompter initiation of bi-fuels compared to CuO/Al (Table 1). Indeed, the low temperature exothermic events (below Al melting) releases more heat compared to that of CuO/Al multilayers: the heat released below 550 °C represent 79.5% and 70.5% of the total heat in CuO/TiB$_2$-Al and CuO/Al-TiB$_2$ systems respectively against only 23% of the total heat in CuO/Al (Table 3). The Al$_x$O$_y$ interface growing in CuO/Al at 400 °C (Fig. 2, region R_2) is therefore a better oxygen diffusion barrier than the native TiO/TiO$_2$ layer [37].

(ii) Exothermic occurrences in CuO/TiB$_2$-Al and CuO/Al-TiB$_2$ multilayer are a superposition of the individual reaction steps recorded in the two reference multilayers, CuO/Al and CuO/TiB$_2$ (Fig. 2, dotted plots) which also happens to be the multilayers releasing maximum heat

Table 3
Approximate heats of reaction determined from the DSC scans.

Sample	Heat of reaction (J/g)		Total heat of reaction (J.g^{-1})
	<550 °C	<650 °C	
CuO/Al	179 ± 3	602 ± 10	1580
CuO/TiB$_2$	740 ± 4	1196 ± 5	1536
CuO/TiB$_2$-Al	764 ± 11	1116 ± 19	1403
CuO/Al-TiB$_2$	730 ± 6	940 ± 7	1035

of reaction: 1780 J.g^{-1} and 1630 J.g^{-1} for CuO/Al and CuO/TiB$_2$, respectively. This indicates that 'hidden' endothermic reactions such as phase transformations which are not detected by XRD occur within the ternary thermite reaction process. Furthermore, some liquid B$_2$O$_3$ may be reduced to B (detected at ∼ 550 °C) when reacting with Al.

(iii) Finally, while the main exothermic reactions in both samples are attributed to the oxidation of titanium, boron, and aluminum, their onset temperature and intensity vary with the deposition sequence: either TiB$_2$ nanolayer deposited prior to Al onto CuO (CuO/TiB$_2$-Al configuration), or TiB$_2$ deposited onto Al over CuO (CuO/Al-TiB$_2$ configuration). This indicates that the nature and the thickness of the interfaces has a significant impact on the ternary thermite reaction process.

Deeper understanding on the reaction of the ternary systems necessitates a morphological as well as chemical analysis, which is addressed next by coupling TEM and EELS, at selected annealing steps. The target temperatures for annealing were set at 475 °C and 550 °C for CuO/TiB$_2$-Al and 375 °C and 480 °C for CuO/Al-TiB$_2$ system because of the DSC traces.

3.3. Morphology and chemical analysis of the bi-fuel samples

3.3.1. As deposited

The Fig. 3a and e show the STEM images of CuO-TiB$_2$-Al-CuO and CuO-Al-TiB$_2$-CuO stacks indicating the respective thicknesses of each layer. CuO layer possesses a thin columnar structure and quite rough surface morphology. The consonant EDX maps of the CuO-TiB$_2$-Al-CuO and CuO-Al-TiB$_2$-CuO stacks (**Figure S4, Supplementary Information**) do not show any severe intermixing close to the interfaces. Fig. 3b-d and f-h show the high-resolution STEM micrographs of each of the resultant interfaces. No voids or delamination are observed between each layer. Al-CuO interface features a 4 ± 0.2 nm thick native alumina formation observed previously [46]. It is worth noting however that the deposition of Al over CuO results in more jagged projections at the interface compared to a relatively smoother interface formed as a result of the deposition of CuO over Al. It has been previously reported that more is the contact surface damage, lower is the probability of quicker oxidation onset [47]. The CuO-TiB$_2$ and TiB$_2$-CuO interfaces are less defined. The inability to discern the formation of a native interface between CuO and TiB$_2$ suggests remarkable resistance of TiB$_2$ to oxidation at room temperature. Note that the deposition of CuO over TiB$_2$ results in less rough interface compared to otherwise. This is attributed to the rough uneven surface of CuO created as a result of columnar growth, into which TiB$_2$ tends to penetrate filling any spaces. The hardly distinguishable Al-TiB$_2$ and TiB$_2$-Al interfaces are observed to be rather compact, the former however being more uniform. Next, the chemical nature of the interfaces is determined by Electron Loss Near Edge Structure (ELNES). Cu L$_{2,3}$-edges at 931–951 eV, O K-edge at 536 eV, B K-edge at 188 eV, Ti L$_{2,3}$-edges at 456–462 eV and Al K-edge at 1560 eV were acquired near and across the unexplored interfaces namely CuO-TiB$_2$, TiB$_2$-CuO, TiB$_2$-Al and Al-TiB$_2$. EELS core loss edges were background subtracted using a power law fit before being plotted in **Figure S5, Supplementary Information**.

Across CuO-TiB$_2$ interface (**Figure S5a**) and close to CuO, sharp B peak at 194 eV along with a second peak at ~204 eV indicates the presence of B-O (as in B$_2$O$_3$) and Ti-B bonds (as in TiB$_2$). Because TiB$_2$ always has two native oxides to its sort, we conjecture the presence of TiO$_x$ as well. Indeed, Ti L$_{2-3}$ edges at 453–465 eV back this occurrence up. Since the two peaks do not show any splitting, they can be attributed to a mixture of Ti^{2+} and Ti^{3+}, which could either be a Ti-B bond or Ti-O bond [37]. The presence of O K-edge however confirms some oxidation in the vicinity of CuO-TiB$_2$ interface.

Interestingly, across the TiB$_2$-CuO interface (**Figure S5b**), slight shift of Ti L$_2$ edge from 456 eV to 457 eV and slight splitting of the oxygen peak points to the formation of a mixture of Ti^{2+} and Ti^{3+} as well. In the vicinity of CuO, a pre-oxygen peak at 529 eV normally attributed to the
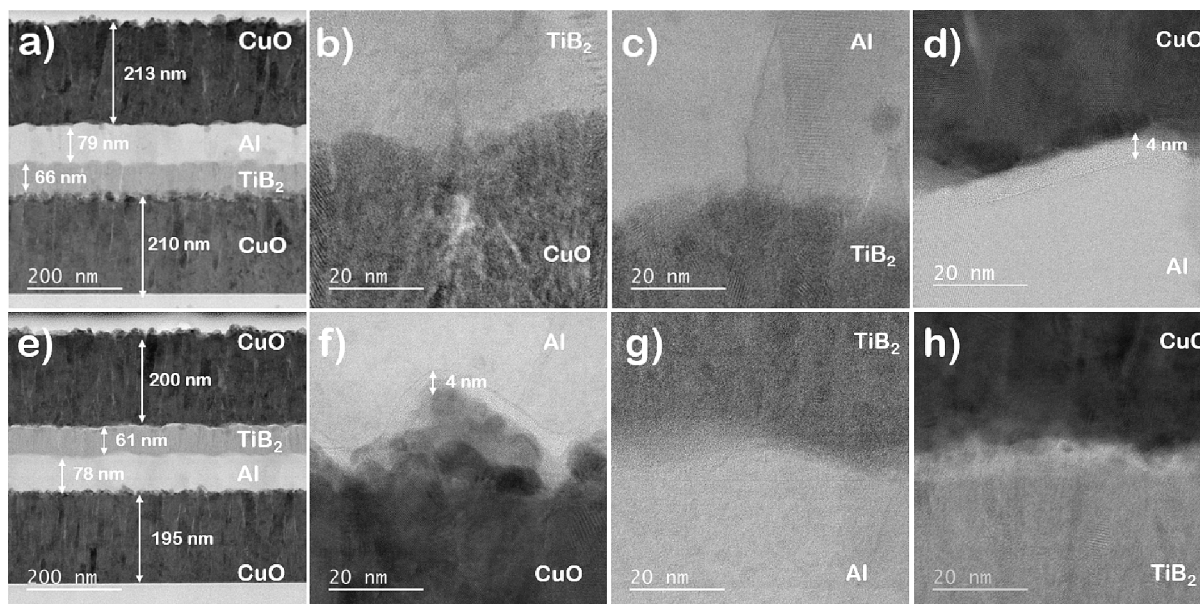
Fig. 3. STEM images showing as deposited multilayers and the corresponding interfaces: **a)** CuO-TiB$_2$-Al-CuO **b)** CuO-TiB$_2$ **c)** TiB$_2$-Al **d)** Al-CuO and **e)** CuO-Al-TiB$_2$-CuO **f)** CuO-Al **g)** Al-TiB$_2$ **h)** TiB$_2$-CuO. All interfaces are observed to be quite dense with no delamination.

presence of molecular oxygen is recorded. In addition, B K edges at 194 eV and a further peak at 204 eV confirms the presence of B-O bond across this interface. This is attributed to the slow outward diffusion of oxygen from CuO as seen previously across CuO-TiB$_2$ interface.

In summary, the CuO-TiB$_2$ and TiB$_2$-CuO interfaces display similar chemical behavior at room temperature except the presence of gaseous oxygen in the latter.

Across TiB$_2$-Al and Al-TiB$_2$ interfaces (**Figure S5b, Supplementary Information**), the L$_{2-3}$ edges at 456–462 eV are attributed to Ti-B bond. While the Al-TiB$_2$ interface features a sharp and clear transition from TiB$_2$ to Al with no detectable elemental intermixing, the TiB$_2$-Al interface shows some Al, Ti and B intermixing. During the sputtering of Al over TiB$_2$ (less compact than Al), the former tends to fill into any empty spaces in TiB$_2$ columns henceforth giving rise to low intensity ELNES of Al, Ti and B in the vicinity of the interface, which is an important difference between both bi-fuel configurations.

3.3.2. Annealed

To investigate the changes in microstructure of each layer as well as the evolution of the interfaces, the two bi-fuel samples were annealed at 475 °C and 550 °C for CuO/TiB$_2$-Al multilayer; and at 375 °C and 480 °C for CuO/Al-TiB$_2$ multilayer based off of the DSC traces. The resulting observations are discussed below.

CuO/TiB$_2$-Al system: Annealing up to 475 °C reduced the thickness of Al by $\sim$ 13% to 69 $\pm$ 2 nm with little morphological changes (Fig. 4a). Interestingly, the thickness of TiB$_2$ went up by $\sim$ 76% to 116 $\pm$ 2 nm introducing porosity in the layer. EDX (**Figure S3b, Supplementary Information**) maps reveal the presence of oxygen throughout TiB$_2$ layer marking the ongoing oxidation process. XRD at this stage showed the presence of TiO$_2$ (**Figure S7a-f, Supplementary Information**). One interesting result of this annealing is the shrinkage of CuO by $\sim$ 37% to 134 $\pm$ 20 nm accompanied by the rapid reduction of CuO to Cu, aggressive enough to create $\sim$ 70 nm deep uneven void (**Figure S6a, Supplementary Information**). This is confirmed by the EDX map (**Figure S7a-f, Supplementary Information**) showing the presence of Cu and no oxygen in the bottommost layer as well as by XRD showing signals from metallic Cu. The oxygen gas liberated as part of this decomposition is quickly adsorbed by TiB$_2$ causing prompt oxidation and the release of most of the heat (Fig. 2, region R$_2$). More interestingly, Cu diffused through the multilayer ascending to TiB$_2$ and Al layers

concentrating at CuO-TiB$_2$ and TiB$_2$-Al interfaces (**Figure S3b and Figure S7e, Supplementary Information**). A thinly undefined $\sim$4 nm CuO-TiB$_2$ interface was left at some areas of contact, while 45 $\pm$ 5 nm TiB$_2$-Al interface exhibited an amorphous dual interfacial formation (**Fig. 4b-c**). The denser bottom layer of this dual interface is concentrated with Cu while the top features the presence of mainly Ti and O, and some Al (weak signals from AlTi seen in the XRD). Al-CuO also featured a 16 $\pm$ 1 nm thick amorphous alumina interface formed as a result of slow Al oxidation (**Fig. 4d**). The ELNES of B, Ti, O, Cu and Al acquired across the TiB$_2$-Al interface annealed at 475 °C (**Figure S9a, Supplementary Information**) confirm the presence of glassy B$_2$O$_3$ as well as oxygen rich TiO (major shift of Ti L$_{2,3}$ edges to 460–466 eV and O K-edge at 532 eV) in accordance with the XRD analysis. Upon closer examination, right at the bottom of TiB$_2$ (near the initially present CuO-TiB$_2$ interface), there is a slight splitting of Ti L edges confirming the occurrence of TiO$_2$ [37,50]. Nevertheless, most of TiB$_2$ happens to be oxidized to TiO. It is only across the TiB$_2$-Al interface that some existence of B is detected closer to Al layer.

Annealing to 550 °C features further reduction of bottom CuO augmenting the void to about 1 μm in depth (**Figure S6b, Supplementary Information**). Cu is not detected in either TiB$_2$ or Al nanolayers anymore. Any oxygen released hereafter is rapidly consumed by TiB$_2$, which features severe porosity furthering its thickness to 133 $\pm$ 4 nm. As shown in the EDX maps, diffused O spans the thickness of TiB$_2$. Additionally, Ti also diffuses through the interfacial oxides into Al causing some intermixing (**Figure S7g-l, Supplementary Information**). Al and the top CuO layers curtailed by 16% and 7% to 58 $\pm$ 16 nm 188 $\pm$ 8 nm respectively. The TiB$_2$-Al and Al-CuO interfaces, widen following a similar nature as observed at lower temperature. It should be noted that B is too light to be detected accurately by EDX but is identified by EELS (**Figure S9b, Supplementary Information**).

CuO/Al-TiB$_2$ system: The microstructural changes in CuO/Al-TiB$_2$ system annealed at 375 °C (**Fig. 4i-l**) and 480 °C (**Fig. 4m-p**) show strikingly different progression of the reaction. While the bottom CuO shows a mere 2% (to 192 $\pm$ 3 nm at 375 °C) and 3% (to 190 $\pm$ 2 nm at 480 °C) reduction in its thickness, the top CuO reduces by 3% at 375 °C and 6% by 480 °C. Its microstructure changes from columnar to slightly granular. The CuO-Al interface features an amorphous alumina confirmed by the EDX maps (**Figure S8c and f, Supplementary Information**), thickness of which increases from an initial 14 nm to 32 nm
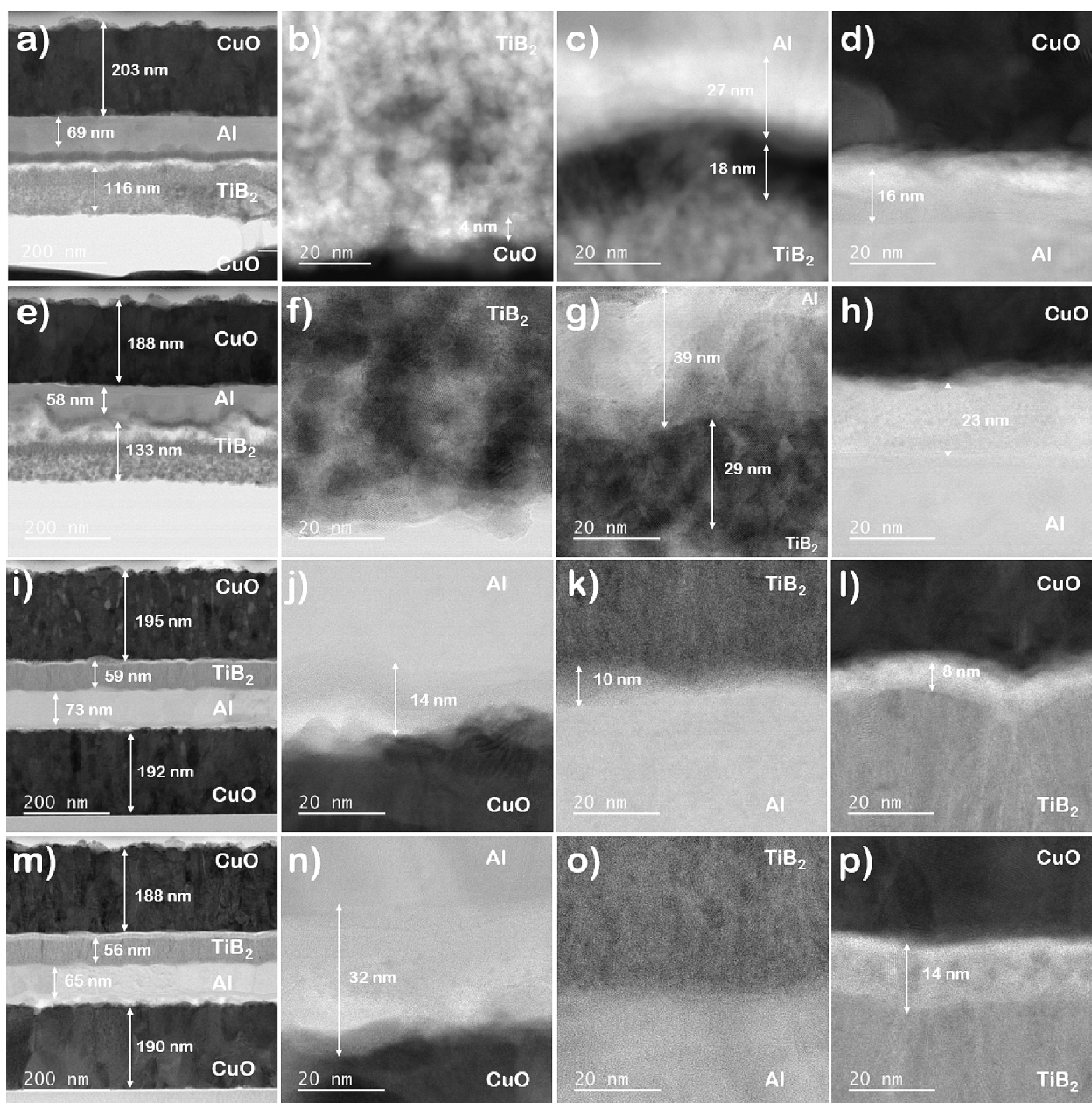
Fig. 4. STEM images showing annealed multilayers and the corresponding interfaces: **a)** CuO-TiB$_2$-Al-CuO annealed at 475 °C and its interfaces **(b-d)**, **e)** CuO-TiB$_2$-Al-CuO annealed at 550 °C and its interfaces **(f-h)**, **i)** CuO-Al-TiB$_2$-CuO annealed at 375 °C and its interfaces **(j-l)**, **m)** CuO-Al-TiB$_2$-CuO annealed at 480 °C and its interfaces **(n-p)**.

showing that Al oxidation did in fact begin at a temperature lower than previously observed [46]. A faster oxidation and subsequent growth at the interface lead to the formation of voids at this interface (**Figure S8g, Supplementary Information**). The thickness of Al reduced by 6% to 73 ± 3 nm at 375 °C and further by 16% to 65 ± 2 nm at 480 °C. TiB$_2$ hardly diminished until 375 °C but depreciated by 8% to 65 ± 2 nm at 480 °C. Al-TiB$_2$ interface is observed to be quite dense with no distinguishable interface, except a ∼ 10 nm interface can be sporadically defined (**Fig. 4k**). A very well defined TiB$_2$-CuO interface mainly composed of Ti and O grows from an initial 8 nm (at 375 °C) to 14 nm (at 480 °C). The ELNES of B, Ti and O acquired across Al-TiB$_2$ interface, at 375 °C and 480 °C (**Figure S10a-b, Supplementary Information**), indicate a change in Ti bonding to Ti-O from an initial Ti-B (high energy-loss shift of Ti L edges to 458–464 eV from an initial 457–462 eV). In addition, there is no oxygen signal picked up close to Al layer suggesting any diffused oxygen is consumed by the adjacent TiB$_2$. ELNES of Ti indicate

the formation of TiO$_2$ and Cu$_2$O at this interface (shift in Ti L edges to 460–466 eV with slight peak splitting in the vicinity of CuO and shift in Cu L edges to higher energy-loss). Close to top CuO, it is worth noting that there is a low intensity B L-edge (onset at 198 eV) as well, but no O K-edge supporting the formation of B$_2$O$_3$. Thus, it may be attributed to elemental B as a result of reaction of B$_2$O$_3$ with Al to produce B and Al$_2$O$_3$. Further annealing to 480 °C, no formation of B$_2$O$_3$ is seen, boron oxide is therefore reduced. The low intensity O K-edges however mark the beginning of oxidation at this interface via outward oxygen ion diffusion from the oxidizer. Quite remarkably, TiB$_2$-CuO interface not only displays the thickening of the interface but also Ti L edges' splitting pointing to the presence of Ti^{4+}. The corresponding splitting in O K edge confirms the presence of stoichiometric TiO$_2$ at this interface. In the vicinity of top CuO, a shift of Cu L edges to higher binding energy indicates the presence of Cu$_2$O, a product of the ongoing redox reaction (**Fig. 2**, region R$_2$). As TiO$_2$ is one of the final reaction products, it seems

like unlike CuO/TiB$_2$-Al, CuO/-Al-TiB$_2$ reaches completion stage faster. It has been shown previously that the presence of TiO$_2$/B$_2$O$_3$ mixture is capable of enhancing oxidation rate by creating alternative oxygen diffusion pathways [51]. Reportedly, CuO/Ti undergoes a two-step redox reaction, first forming TiO at lower temperature and finally to TiO$_2$ at ~500 °C [37]. It seems TiB$_2$ follows a similar regime except in the binary fuels, in addition, it facilitates CuO/Al main reaction to begin earlier as well.

3.4. Discussions and reaction scenario

STEM-EELS for the different temperature stages coupled with DSC, XRD and EDX revealed:

i. *Strong affinity of TiB$_2$ to oxygen that catalyzes CuO decomposition:* TiB$_2$ in direct contact with CuO boosted the latter's decomposition at temperatures as low as 380 °C.

ii. *TiB$_2$ dissociation and further Ti and B oxidation:* Owing to the oxygen release from CuO, Ti-B bonds break, enabling Ti and B to oxidize to TiO$_x$ and B$_2$O$_3$ at ~300 °C and 410 °C respectively. Note that the Ti-B bond dissociation energy is 272 kJ.mol^{-1} against 820 kJ.mol^{-1} and 670 kJ.mol^{-1} for B-O and Ti-O bonds respectively. This additionally explains the low auto-ignition point of CuO/TiB$_2$ thermite.

iii. *Reduction of liquid B$_2$O$_3$ in contact with Al:* Some elemental boron is detected at temperatures > 550 °C (post region R$_2$, Fig. 2) likely caused by the reduction of liquid B$_2$O$_3$ (melting point of 450 °C) in contact with Al.

iv. *Oxidation of Al post melting:* The ultimate reaction stage is the oxidation of metallic aluminum with the remaining oxygen (R$_3$, Fig. 2).

The reaction steps are thus tabulated below:

Table 4
Reactional steps in the ternary CuO/Al-TiB$_2$ nanothermite system.

Step I	$2\ CuO\ (s) \rightarrow Cu_2O\ (s) + ½\ O_2\ (g)$
	$Cu_2O\ (s) + ½\ O_2\ (g) \rightarrow 2\ Cu\ (s) + O_2\ (g)$
Step II	$TiB_2\ (s) + 2\ O_2\ (g) \rightarrow TiO\ (s) + B_2O_3\ (s)$
	$Ti\ (s) + 2\ O_2\ (g) \rightarrow TiO_2\ (g)$
	$TiO\ (s) + ½\ O_2\ (g) \rightarrow TiO_2\ (s)$
	$2\ B\ (s) + 3/2\ O_2\ (g) \rightarrow B_2O_3\ (s)$
Step III	$2\ Al\ (s) + B_2O_3\ (l) \rightarrow Al_2O_3\ (s) + 2B\ (s)$
	$2\ Al\ (s) + 3\ O_2\ (g) \rightarrow Al_2O_3\ (s)$

Importantly, STEM-EELS also allowed to depict the differences in the performances of CuO/TiB$_2$-Al versus CuO/Al-TiB$_2$ systems. In the former, i.e., when Al is sputtered onto TiB$_2$, Al is seen to migrate into the perpendicular columns of TiB$_2$ which penalizes its reactivity. We
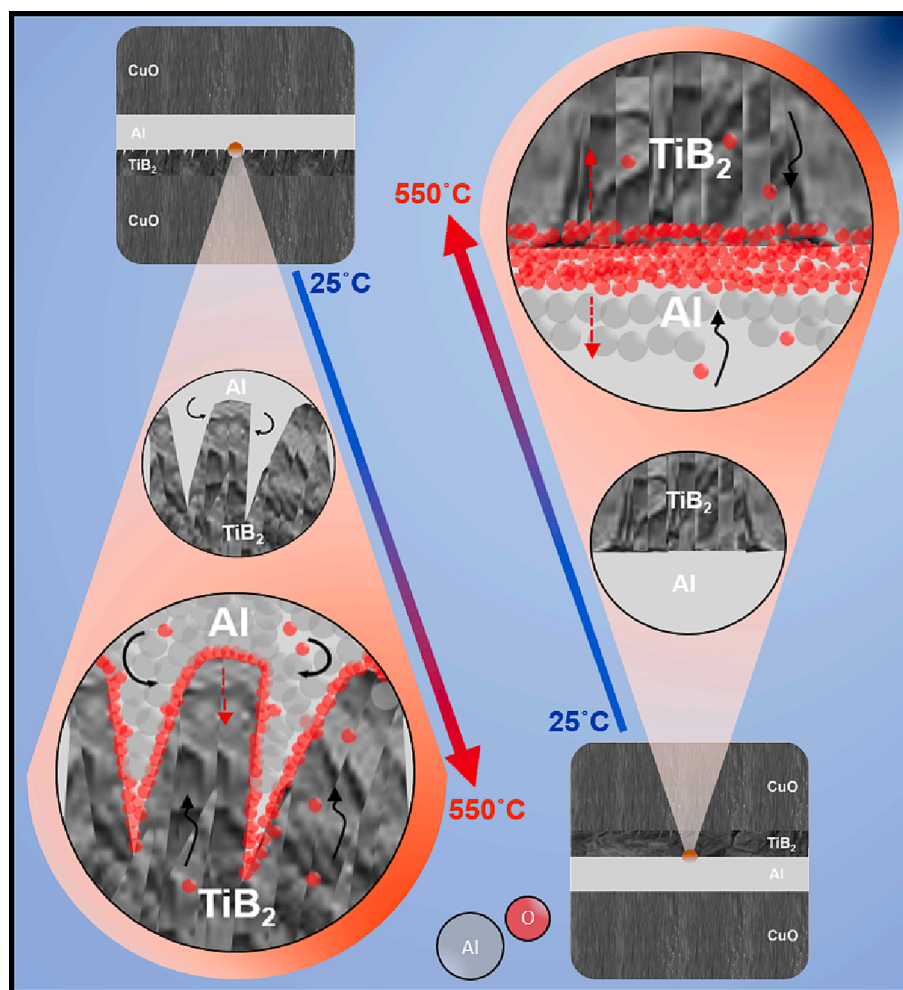

Fig. 5. Schematic of an outlook on the oxidation and potential microstructural changes of TiB$_2$-Al and Al-TiB$_2$ interfaces. While the oxide layer (in red) can grow bidirectionally in CuO-Al-TiB$_2$-CuO, CuO-TiB$_2$-Al-CuO features a unidirectional oxide growth which is inhibited by Al due to the lower probability of Al-O bond formation than that of Ti-O.

observed that TiB$_2$ possesses a very small grain size compared to Al and is characterized by less dense columnar morphology. When Al is deposited over TiB$_2$, it tends to fill into any crevices (**Fig. 3a** and **e)**. Then upon annealing, when oxidation begins as a result of oxygen ion diffusion, the alumina layer formed at the boundaries prevent oxygen movement through the underneath TiO$_x$ inhibiting oxidation as the temperature increases [52]. The schematic of the mechanism taking place at sufficiently high temperatures (>550 °C) is shown in Fig. 5. Moreover, the delamination behavior as well as nano-structural losses in CuO/TiB$_2$-Al at temperatures as low as ~ 475 °C may hinder and/or delay chemical exchanges/reactions provides another potential explanation for its lower performance in comparison to CuO/Al-TiB$_2$. This severity of the damage in the nanostructure simply comes from the direct CuO-TiB$_2$ contact that then results in rapid oxidizer consumption. As a premise of this phenomenon, a 2 BL CuO/TiB$_2$ was annealed to 550 °C and the resulting TEM micrographs (**Figure S11, Supplementary Information**) exhibited similarly destroyed nanolaminate.

4. Conclusion

The effect of TiB$_2$ as an additive thin film on the initiation and the combustion properties of CuO/Al multilayers was studied. The CuO/TiB$_2$-Al and CuO/Al-TiB$_2$ multilayers demonstrated much higher burn rates of 8.3 m.s^{-1} and 10.8 m.s^{-1} respectively, compared to that of CuO/Al and CuO/TiB$_2$, which burn at 4.3 m.s^{-1} and 2.2 m.s^{-1}, respectively. The additive TiB$_2$ not only enhances the burn rate by ~ 50% compared to the CuO/Al reference sample but also exhibited ~ 100% lower ignition energy of 1.3 mJ (CuO/TiB$_2$-Al) and 0.033 mJ (CuO/Al-TiB$_2$) in comparison to unary fuel-based multilayers. Overall, this study shines light upon the utility of TiB$_2$ as an additive thin film to realize the ultimate goal of enhancing the ignitability and burn rate of CuO/Al thermites. The results demonstrated (i) a strong affinity of TiB$_2$ to oxygen that enhances CuO decomposition at temperature as low as 380 °C; (ii) a concomitant TiB$_2$ oxidation, to TiO, and B$_2$O$_3$; (iii) continuation of Ti oxidation into TiO$_2$ depending upon the availability of the oxidizer; (iv) Al oxidation at high temperatures via liquid B$_2$O$_3$ as well as remaining gaseous oxygen. This study also highlights the criticality of the order of stacking of metallic layer in nanothermites. The reaction in CuO/Al-TiB$_2$ system was found to evolve rapider than CuO/TiB$_2$-Al (auto-ignition point is 380 °C against 445 °C for CuO/Al-TiB$_2$) but propagate less aggressively (slower flame propagation) due to the presence of Al in the TiB$_2$ grain boundaries which degrades the reactivity.

Declaration of Competing Interest

The authors declare that they have no known competing financial interests or personal relationships that could have appeared to influence the work reported in this paper.

Data availability

No data was used for the research described in the article.

Appendix A. Supplementary data

Supplementary data to this article can be found online at https://doi.org/10.1016/j.fuel.2023.128599.

References

[1] Dreizin EL, Schoenitz M. Mechanochemically prepared reactive and energetic materials: a review. J Mater Sci 2017;52(20):11789–809. https://doi.org/10.1007/s10853-017-0912-1.

[2] Yetter RA, Risha GA, Son SF. Metal particle combustion and nanotechnology. Proc Combust Inst 2009;32(2):1819–38. https://doi.org/10.1016/j.proci.2008.08.013.

[3] Liang D, Liu J, Xiao J, Xi J, Wang Y, Zhou J. Effect of metal additives on the composition and combustion characteristics of primary combustion products of B-based propellants. J Therm Anal Calorim 2015;122(1):497–508. https://doi.org/10.1007/s10973-015-4750-6.

[4] Zhu C-G, Wang H-Z, Min L. Ignition temperature of magnesium powder and pyrotechnic composition. J Energ Mater 2014;32(3):219–26.

[5] Levashov E, Mukasyan A, Rogachev A, Shtansky D. Self-propagating high-temperature synthesis of advanced materials and coatings. Int Mater Rev 2016;62:1–37. https://doi.org/10.1080/09506608.2016.1243291.

[6] Wang LL, Munir ZA, Maximov YM. Thermite reactions: their utilization in the synthesis and processing of materials. J Mater Sci 1993;28(14):3693–708. https://doi.org/10.1007/BF00353167.

[7] Troianello T. Precision Foil Resistors Used as Electro-Pyrotechnic Initiators. In *2001 Proceedings. 51st Electronic Components and Technology Conference (Cat. No.01CH37220)*; 2001; pp 1413–1417. https://doi.org/10.1109/ECTC.2001.928019.

[8] Jr TWB, Simpson RL, Gash AE, Jr JHS. Nano-Laminate-Based Ignitors. US7951247B2, May 31, 2011. https://patents.google.com/patent/US7951247B2/en (accessed 2022-11-13).

[9] Kang X, Zhang J, Zhang Q, Du K, Tang Y. Studies on ignition and afterburning processes of KClO$_4$/Mg pyrotechnics heated in air. J Therm Anal Calorim 2012;109(3):1333–40. https://doi.org/10.1007/s10973-011-1991-x.

[10] Fu S, Shen R, Zhu P, Ye Y. Metal–interlayer–metal structured initiator containing Al/CuO reactive multilayer films that exhibits improved ignition properties. Sens Actuators, A 2019;292:198–204. https://doi.org/10.1016/j.sna.2019.04.019.

[11] Ahn JY, Kim SB, Kim JH, Jang NS, Kim DH, Lee HW, et al. A micro-chip initiator with controlled combustion reactivity realized by integrating Al/CuO nanothermite composites on a microhotplate platform. J Micromech Microeng 2015;26(1):015002. https://doi.org/10.1088/0960-1317/26/1/015002.

[12] Pouchairet J-L, Rossi C. PyroMEMS as future technological building blocks for advanced microenergetic systems. Micromachines 2021;12(2):118. https://doi.org/10.3390/mi12020118.

[13] Nicollet A, Lahiner G, Belisario A, Souleille S, Djafari-Rouhani M, Estève A, et al. Investigation of Al/CuO multilayered thermite ignition. J Appl Phys 2017;121(3):034503. https://doi.org/10.1063/1.4974288.

[14] Bockmon B, Pantoya M, Son S, Asay B. Burn Rate Measurements of Nanocomposite Thermites. In *41st Aerospace Sciences Meeting and Exhibit*; American Institute of Aeronautics and Astronautics. https://doi.org/10.2514/6.2003-241.

[15] Li S, Guo T, Yao M, Song J, Ding W, Mao Y, et al. Effect of bismuth oxide particles size on the thermal excitation and combustion properties of thermite systems. ChemistryOpen 2021;10(4):464–70. https://doi.org/10.1002/open.202000358.

[16] Weir C, Pantoya ML, Daniels MA. The role of aluminum particle size in electrostatic ignition sensitivity of composite energetic materials. Combust Flame 2013;160(10):2279–81. https://doi.org/10.1016/j.combustflame.2013.05.005.

[17] Rossi C. Engineering of Al/CuO reactive multilayer thin films for tunable initiation and actuation. Prop, Explos Pyrotech 2019;44(1):94–108. https://doi.org/10.1002/prep.201800045.

[18] Wu T, Lahiner G, Tenailleau C, Reig B, Hungria T, Esteve A, et al. Unexpected enhanced reactivity of aluminized nanothermites by accelerated aging. Chem Eng J 2021;418:129432.

[19] Wang H, Julien B, Kline DJ, Alibay Z, Rehwoldt MC, Rossi C, et al. Probing the reaction zone of nanolaminates at ~μs Time and ~μm spatial resolution. J Phys Chem C 2020;124(25):13679–87. https://doi.org/10.1021/acs.jpcc.0c01647.

[20] Meda L, Marra G, Galfetti L, Severini F, De Luca L. Nano-aluminum as energetic material for rocket propellants. Mater Sci Eng C 2007;27(5):1393–6. https://doi.org/10.1016/j.msec.2006.09.030.

[21] Yetter RA. Progress towards nanoengineered energetic materials. Proc Combust Inst 2021;38(1):57–81.

[22] Aly Y, Schoenitz M, Dreizin EL. Aluminum-metal reactive composites. Combust Sci Technol 2011;183(10):1107–32. https://doi.org/10.1080/00102202.2011.584090.

[23] DeLuca LT. Overview of Al-based nanoenergetic ingredients for solid rocket propulsion. Defence Technol 2018;14(5):357–65. https://doi.org/10.1016/j.dt.2018.06.005.

[24] Ma X, Li Y, Hussain I, Shen R, Yang G, Zhang K. Core-shell structured nanoenergetic materials: preparation and fundamental properties. Adv Mater 2020;32(30):2001291. https://doi.org/10.1002/adma.202001291.

[25] Sambamurthi JK, Price EW, Sigman RK. Aluminum agglomeration in solid-propellant combustion. AIAA J 1984;22(8):1132–8. https://doi.org/10.2514/3.48552.

[26] Cohen NS. A Pocket model for aluminum agglomeration in composite propellants. AIAA J 1983;21(5):720–5. https://doi.org/10.2514/3.8139.

[27] Wang H, Kline DJ, Zachariah MR. In-operando high-speed microscopy and thermometry of reaction propagation and sintering in a nanocomposite. Nat Commun 2019;10(1):3032. https://doi.org/10.1038/s41467-019-10843-4.

[28] Sullivan KT, Piekiel NW, Wu C, Chowdhury S, Kelly ST, Hufnagel TC, et al. Reactive sintering: an important component in the combustion of nanocomposite thermites. Combust Flame 2012;159(1):2–15. https://doi.org/10.1016/j.combustflame.2011.07.015.

[29] Chakraborty P, Zachariah MR. Do nanoenergetic particles remain nano-sized during combustion? Combust Flame 2014;161(5):1408–16. https://doi.org/10.1016/j.combustflame.2013.10.017.

[30] Aly Y, Dreizin EL. Ignition and combustion of Al·Mg alloy powders prepared by different techniques. Combust Flame 2015;162(4):1440–7. https://doi.org/10.1016/j.combustflame.2014.11.010.

[31] Aly Y, Schoenitz M, Dreizin EL. Ignition and combustion of mechanically alloyed Al–Mg powders with customized particle sizes. Combust Flame 2013;160(4):835–42. https://doi.org/10.1016/j.combustflame.2012.12.011.

[32] Hastings D, Rodriguez N, McCann H, Schoenitz M, Dreizin EL. Titanium-boron reactive composite powders with variable morphology prepared by arrested reactive milling. Fuel 2022;310:122313. https://doi.org/10.1016/j.fuel.2021.122313.

[33] Chiu LH, Nagle DC, Bonney LA. Thermal analysis of self-propagating high-temperature reactions in titanium, boron, and aluminum powder compacts. *Metall Mater Trans A* 8.

[34] Vummidi Lakshman S, Gibbins JD, Wainwright ER, Weihs TP. The effect of chemical composition and milling conditions on composite microstructure and ignition thresholds of AlZr ball milled powders. Powder Technol 2019;343:87–94. https://doi.org/10.1016/j.powtec.2018.11.012.

[35] Wainwright ER, Weihs TP. Microstructure and ignition mechanisms of reactive aluminum-zirconium ball milled composite metal powders as a function of particle size. J Mater Sci 2020;55(29):14243–63. https://doi.org/10.1007/s10853-020-05031-5.

[36] Shoshin YL, Dreizin EL. Particle combustion rates for mechanically alloyed Al–Ti and aluminum powders burning in air. Combust Flame 2006;145(4):714–22. https://doi.org/10.1016/j.combustflame.2005.11.006.

[37] Wu T, Singh V, Julien B, Tenailleau C, Estève A, Rossi C. Pioneering insights into the superior performance of titanium as a fuel in energetic materials. Chem Eng J 2023;453:139922. https://doi.org/10.1016/j.cej.2022.139922.

[38] Gany A, Netzer DW. Combustion studies of metallized fuels for solid-fuel ramjets. J Propul Power 1986;2(5):423–7. https://doi.org/10.2514/3.22924.

[39] MACEK A, SEMPLE J. Combustion of Boron Particles at Atmospheric Pressure. In *5th Propulsion Joint Specialist*; American Institute of Aeronautics and Astronautics. https://doi.org/10.2514/6.1969-562.

[40] Guo W, Chang S, Cao J, Wu L, Shen R, Ye Y. Precisely controlled reactive multilayer films with excellent energy release property for laser-induced ignition. Nanoscale Res Lett 2019;14(1):301. https://doi.org/10.1186/s11671-019-3124-6.

[41] Zapata J, Nicollet A, Julien B, Lahiner G, Esteve A, Rossi C. Self-propagating combustion of sputter-deposited Al/CuO nanolaminates. Combust Flame 2019;205:389–96. https://doi.org/10.1016/j.combustflame.2019.04.031.

[42] Adams DP. Reactive multilayers fabricated by vapor deposition: a critical review. Thin Solid Films 2015;576:98–128. https://doi.org/10.1016/j.tsf.2014.09.042.

[43] Salvagnac L, Assie-Souleille S, Rossi C. Layered Al/CuO thin films for tunable ignition and actuations. Nanomaterials 2020;10(10):2009. https://doi.org/10.3390/nano10102009.

[44] Julien B, Dubreuil P, Josse C, Salvagnac L, Pelloquin S, Esteve A, et al. Effect of substrate-induced localized stress on the combustion properties of Al/CuO reactive multilayer films. Thin Solid Films 2021;740:139000. https://doi.org/10.1016/j.tsf.2021.139000.

[45] Weihs TP. Self-Propagating Reactions in Multilayer Materials. In *Handbook of Thin Film Process Technology*; D.A. Glocker, S.I. Shah, Eds.; IOP Publishing, 1998.

[46] Singh V, Julien B, Salvagnac L, Pelloquin S, Hungria T, Josse C, et al. Influence of process parameters on energetic properties of sputter-deposited Al/CuO reactive multilayers. Nanotechnology 2022;33(46):465704.

[47] Biswas P, Xu F, Ghildiyal P, Zachariah MR. In-situ thermochemical shock-induced stress at the metal/oxide interface enhances reactivity of aluminum nanoparticles. ACS Appl Mater Interfaces 2022;14(23):26782–90. https://doi.org/10.1021/acsami.2c05412.

[48] Marín L, Nanayakkara CE, Veyan J-F, Warot-Fonrose B, Joulie S, Estève A, et al. Enhancing the reactivity of Al/CuO nanolaminates by Cu incorporation at the interfaces. ACS Appl Mater Interfaces 2015;7(22):11713–8. https://doi.org/10.1021/acsami.5b02653.

[49] Julien B, Cure J, Salvagnac L, Josse C, Esteve A, Rossi C. Integration of gold nanoparticles to modulate the ignitability of nanothermite films. ACS Appl Nano Mater 2020;3(3):2562–72. https://doi.org/10.1021/acsanm.9b02619.

[50] Mitterbauer C, Kothleitner G, Hofer F. Comparative electron energy-loss near-edge fine structure investigations of titanium oxides. Microsc Microanal 2003;9(S02):834–5. https://doi.org/10.1017/S1431927603444176.

[51] Zhao W, Wang H, Kline DJ, Wang X, Wu T, Xu J, et al. Influence of titanium addition on performance of boron-based thermites. Chem Eng J 2022;438:134837. https://doi.org/10.1016/j.cej.2022.134837.

[52] Bakhit B, Palisaitis J, Thörnberg J, Rosen J, Persson POÅ, Hultman L, et al. Improving the high-temperature oxidation resistance of TiB2 thin films by alloying with Al. Acta Mater 2020;196:677–89. https://doi.org/10.1016/j.actamat.2020.07.025.